The Effect of Dynamic Range Alterations in the Estimation of Contrast

Ole Marius Hoel Rindal, *Student Member, IEEE*, Andreas Austeng, *Senior Member, IEEE*, Ali Fatemi, *Graduate Student Member, IEEE*, and Alfonso Rodriguez-Molares, *Member, IEEE*

Abstract—**Many adaptive beamformers claim to produce images with increased contrast, a feature that could enable a better detection of lesions and anatomical structures. Contrast is often quantified using the contrast ratio (CR) and the contrast-to-noise ratio (CNR). The estimation of CR and CNR can be affected by dynamic range alterations (DRAs), such as those produced by a trivial gray-level transformation. Thus, we can form the hypothesis that contrast improvements from adaptive beamformers can, partly, be due to DRA. In this paper, we confirm this hypothesis. We show evidence on the influence of DRA on the estimation of CR and CNR and on the fact that several methods in the state of the art do alter the DR. To study this phenomenon, we propose a DR test (DRT) to estimate the degree of DRA and we apply it to seven beamforming methods. We show that CR improvements correlate with DRT with R^2-adj = 0.88 in simulated data and R^2-adj = 0.98 in experiments. We also show that DRA may lead to increased CNR values, under some circumstances. These results suggest that claims on lesion detectability, based on CR and CNR values, should be revised.**

Index Terms—**Adaptive beamforming, Capon's minimum variance, coherence factor, contrast metrics, dynamic range, eigenspace-based minimum variance, filtered-delay multiply and sum, generalized coherence factor, phase coherence factor.**

I. INTRODUCTION

THE popularization of software beamforming has brought numerous techniques that, by clever manipulation of channel data, are able to exceed the contrast and resolution provided by conventional delay-and-sum (DAS) beamforming. We refer as adaptive beamforming to any technique where the signal values alter the way the beamformed signal is constructed, for instance, when the element weights are determined from the variance of the signal.

Seminal work on adaptive beamforming dates back to the 1960s, where optimal element weights were derived for a given signal direction to minimize the influence of jamming signals in radio communication systems [1]–[4].

Adaptive beamforming was first applied to medical ultrasound at the end of the 1980s to compensate for phase aberration artifacts produced by tissue inhomogeneities [5], [6] and about a decade later to reduce the contribution of off-axis targets [7]–[11]. Since then, the number of articles on adaptive beamforming has increased exponentially [12].

Among the alleged benefits of adaptive techniques is that of producing increased contrast, a feature that is often associated with higher lesion detectability. Extraordinary increases in contrast ratio (CR), and in the contrast-to-noise ratio (CNR), with respect to DAS, are reported in the literature [13]–[18].

Another way of increasing the image contrast is by altering the dynamic range (DR) of the beamformed images. This is achieved, for instance, by applying a gray-level transform on the image intensity values which can stretch or compress the DR. Gray-level transforms have traditionally been used in commercial scanners to emphasize certain characteristics of the investigated tissues. This operation does not provide new information or better lesion detection, but it can increase the apparent contrast of the image. This has been known for some time, and it has previously been stated that "any nonlinear postprocessing [...] would be merely cosmetic," and that it "does not affect the intrinsic detectability of low contrast lesions, [...] at least for the ideal observer" and only "slight gains for real observers" [19]. However, these findings seem to be forgotten in the modern ultrasound community. The question then arises on whether some of the alleged benefits of adaptive beamforming could be explained by a DR transformation that is unaccounted for. If that is the case, then some of the reported values for CR and CNR in the literature should be revised.

Rindal *et al.* [20] proposed a phantom to measure the output DR produced by any beamforming algorithm. Using synthetic data, we showed that some adaptive algorithms seem to transform the DR, which, in turn, affected the estimated CR values. Here, we extend the analysis to CNR, include four additional adaptive beamforming techniques, include the effect on vertical gradients, and validate the result with experimental data. We also define a DR test (DRT) that makes it possible to quantify the degree of DR alterations.

In Section II, we present the algorithms under study. In Section III, we review the current contrast quality metrics, present the DR phantoms used both in simulation and in experiments, describe data processing, and introduce the DRT. Results are presented in Section IV and discussed
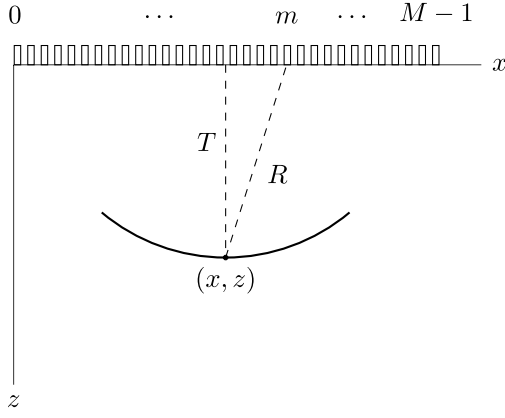
Fig. 1. Geometrical illustration of the posed scenario.

in Section V. Conclusions and further work are included in Section VI.

II. THEORY

Without loss of generality, let us assume a linear array of M elements, laying on the x-axis, pointing toward the positive direction of the z-axis, as illustrated in Fig. 1. The domain, with characteristic sound speed c_0, is illuminated by a generic transmit beam, either planar, converging or diverging. Let us denote the signal received by element m as $h_m(t)$. Let us denote as T the distance from the origin of the transmitted wave to the point (x, z), and as R the distance from (x, z) to the location of element m. If we apply the propagation delay, $\Delta t = (T + R)/c_0$, we obtain the signal value at (x, z) received by element m

$$s_m = h_m(t)|_{t=\Delta t} \tag{1}$$

also referred to as *pixel value*. Note that we drop the spatial coordinates (x, z). The symbol s_m refers to the pixel value at an arbitrary location (x, z), unless otherwise specified.

A. Delay-and-Sum (DAS)

The conventional DAS implementation is the coherent combination of the pixel values as received by all elements, yielding

$$b_{\text{DAS}} = \sum_{m=0}^{M-1} w_m s_m \tag{2}$$

where w_m is the received apodization, a static term often determined from the F-number and the pixel depth z. Equation (2) can be written in algebraic form as

$$b_{\text{DAS}} = \boldsymbol{w}^H \boldsymbol{s} \tag{3}$$

where $\boldsymbol{s} = [s_0 \ s_1 \ \dots \ s_{M-1}]$ is a vector containing the pixel value for every channel in the system.

B. Capon's Minimum Variance (MV)

Capon's minimum variance (MV) technique calculates a data dependent set of weights $\boldsymbol{w}$ while maintaining a unity gain

in the steering direction [21]. This is posed as a minimization problem by

$$\min_{\boldsymbol{w}} \ E\{|b_{\text{DAS}}|^2\} = \boldsymbol{w}^H \boldsymbol{R} \boldsymbol{w}$$
$$\text{s.t. } \boldsymbol{w}^H \boldsymbol{a} = 1 \tag{4}$$

where $\boldsymbol{R} \equiv E\{\boldsymbol{s}\boldsymbol{s}^H\}$ is the spatial covariance matrix, E is the expected value operator, and the steering vector $\boldsymbol{a} = \boldsymbol{1}$ because it is assumed that all signals are already delayed. The solution to (4) can be found by the method of Lagrange multipliers, yielding

$$\boldsymbol{w}_{\text{MV}} = \frac{\boldsymbol{R}^{-1}\boldsymbol{a}}{\boldsymbol{a}^H \boldsymbol{R}^{-1}\boldsymbol{a}}. \tag{5}$$

The spatial covariance matrix is unknown, but it can be estimated for point (x, z), assuming a linear array, by [21]

$$\hat{\boldsymbol{R}}(x, z) = \frac{\sum_{k=-K}^{K} \sum_{l=0}^{M-L} \bar{\boldsymbol{s}}_l(x, z-k)\bar{\boldsymbol{s}}_l^H(x, z-k)}{(2K+1)(M-L+1)} \tag{6}$$

where $(2K+1)$ is the number of axial samples, L is the length of the subarray, and

$$\bar{\boldsymbol{s}}_l(x, z) = [s_l(x, z) \ \ s_{l+1}(x, z) \ \ \dots \ \ s_{l+L-1}(x, z)]^T. \tag{7}$$

The subarray averaging improves robustness. To further improve robustness, and numerical stability, diagonal loading is added to the estimated covariance matrix by $\tilde{\boldsymbol{R}}(x, z) = \hat{\boldsymbol{R}}(x, z) + \epsilon \mathbf{I}$, where $\mathbf{I}$ is the identity matrix, and

$$\epsilon = \frac{\Delta}{L} \text{tr}\{\hat{\boldsymbol{R}}(x, z)\}$$

where tr{} is the trace operator.

The beamformed image is then computed as

$$b_{\text{MV}} = \frac{1}{M-L+1} \sum_{l=0}^{M-L} \boldsymbol{w}_{\text{MV}}^H \bar{\boldsymbol{s}}_l. \tag{8}$$

C. Eigenspace-Based Minimum Variance (EBMV)

The MV can be extended into eigenspace-based minimum variance (EBMV). Asl and Mahloojifar [22] were the first to apply it to beamforming for medical ultrasound. They utilized the eigenstructure of the covariance matrix aiming to obtain a better suppression of off-axis signals. The covariance matrix is estimated with (6) and eigendecomposed as

$$\hat{\boldsymbol{R}}_{\text{DL}} = \boldsymbol{V} \boldsymbol{\Lambda}^{-1} \boldsymbol{V}^H \tag{9}$$

where $\boldsymbol{\Lambda} = [\lambda_1, \lambda_2, \dots, \lambda_L]^T$ are the eigenvalues in descending order, and $\boldsymbol{V} = [\boldsymbol{v}_1, \boldsymbol{v}_2, \dots \boldsymbol{v}_L]$ are the corresponding eigenvectors. The signal subspace $\boldsymbol{E}_s$ can be constructed using the eigenvectors corresponding to the largest eigenvalues

$$\boldsymbol{E}_s = [\boldsymbol{v}_1, \dots, \boldsymbol{v}_E] \tag{10}$$

where E is the number of eigenvectors creating the signal subspace. Finally, the EBMV weight is obtained by projecting the conventional MV weights onto the constructed signal subspace

$$\boldsymbol{w}_{\text{EBMV}} = \boldsymbol{E}_s \boldsymbol{E}_s^H \boldsymbol{w}_{\text{MV}}. \tag{11}$$

The beamformed image is then computed as

$$b_{\text{EBMV}} = \frac{1}{M - L + 1} \sum_{l=0}^{M-L} \boldsymbol{w}_{\text{EBMV}}^{H} \bar{\boldsymbol{s}}_l \qquad (12)$$

with $\bar{\boldsymbol{s}}_l$ defined as in (7).

D. Filtered-Delay Multiply and Sum (F-DMAS)

Filtered-delay multiply and sum (F-DMAS) for medical ultrasound beamforming was introduced by Matrone *et al.* [23]. The technique aims to increase the image quality by multiplying the RF signals before summation. Namely, the signed square root signal is defined as

$$g_{ij} = \text{sign}\left(s_i s_j\right) \sqrt{\left|s_i s_j\right|} \qquad (13)$$

where sign($\cdot$) denotes the sign function. The beamformed signal $b_{\text{F-DMAS}}$ is then computed as

$$b_{\text{F-DMAS}} = \left[\sum_{i=0}^{M-2} \sum_{j=i+1}^{M-1} g_{ij} \right]_{\text{BPF}} \qquad (14)$$

where $[\cdot]_{\text{BPF}}$ denotes the bandpass filtering of the signal inside the brackets. Note that (13) is the multiplication of two signals with identical center frequency f_c, and hence, it will have two frequency components: one at 0, and one at $2f_c$. Bandpass filtering is applied to remove the dc component.

E. Coherence Factor (CF)

The coherence factor (CF) was first introduced by Mallart and Fink [24], as the ratio between the coherent and incoherent energy across the aperture

$$\text{CF} = \frac{\left|\sum_{m=0}^{M-1} s_m\right|^2}{M \sum_{m=0}^{M-1} |s_m|^2}. \qquad (15)$$

The CF has been used as an adaptive weight to increase the image quality [25] as

$$b_{\text{CF}} = \text{CF} b_{\text{DAS}}. \qquad (16)$$

F. Generalized Coherence Factor (GCF)

Li and Li [25] generalized the CF as

$$\text{GCF} = \frac{\sum_{n < M_0} |S_n|^2}{\sum_{n=-\frac{M}{2}}^{\frac{M}{2}-1} |S_n|^2} \qquad (17)$$

where S is the M-point Fourier spectra over the aperture of the delayed channel data

$$S_n = \sum_{m=0}^{M-1} s_m e^{-j2\pi(m-M/2)d\frac{n}{Md}} \qquad (18)$$

where $n \in [-(M/2), (M/2)-1]$ is the spatial frequency index, and M is assumed to be even, d is the pitch of the array, and M_0 is an arbitrary constant within $[0, (M/2) - 1]$ that specifies the low spatial frequency region, thus going from $-M_0$ to M_0. Note that if $M_0 = 0$ the GCF simplifies to the CF.

The beamformed image is computed by multiplying the DAS image with GCF
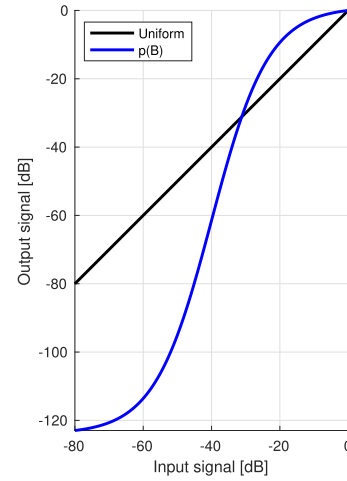
$$b_{\text{GCF}} = \text{GCF} b_{\text{DAS}}. \qquad (19)$$

Fig. 2. Gray-level transform (GLT) S-curve (24) in *log space*.

G. Phase Coherence Factor (PCF)

The PCF was introduced by Camacho *et al.* [26] as

$$\text{PCF} = \max\left\{0, 1 - \frac{\gamma}{\sigma_0} p\right\} \qquad (20)$$

where γ is a parameter to adjust the sensitivity of PCF to out-of-focus signals, $\sigma_0 = \pi/\sqrt{3}$ is the nominal standard deviation of a uniform distribution between $-\pi$ and π, and p is given by

$$p = \min\{\sigma(\boldsymbol{\phi}), \sigma(\boldsymbol{\phi}^A)\} \qquad (21)$$

where $\boldsymbol{\phi} = [\phi_1 \, \phi_2 \ldots \phi_M]$ is the instantaneous phase across the aperture, and $\sigma(\boldsymbol{\phi})$ is its standard deviation. To avoid phase wrapping discontinuity, a set of auxiliary phases $\boldsymbol{\phi}^A = [\phi_1^A \, \phi_2^A \ldots \phi_M^A]$ is computed as

$$\phi_m^A = \begin{cases} \phi_m + \pi, & \text{if } \phi_m < 0 \\ \phi_m - \pi, & \text{otherwise.} \end{cases} \qquad (22)$$

The beamformed image is computed using PCF as an adaptive weight

$$b_{\text{PCF}} = \text{PCF} b_{\text{DAS}}. \qquad (23)$$

H. Gray-Level Transform (GLT)

For completeness, we include a GLT to illustrate how a trivial transformation of the DR can affect the estimation of contrast. In particular, beamformed images are transformed using a sigmoid function (S-curve)

$$\hat{p}(B) = \frac{1}{1 + e^{-\alpha(B-\beta)}} \qquad (24)$$

$$p(B) = \frac{\hat{p}(B) - \max\left(\hat{p}(B)\right)}{\epsilon} \qquad (25)$$

where the coefficients α, β, and ϵ are defined in Section III-D, and where $B = 20\log_{10}(|b_{\text{DAS}}|)$. The plot of the S-curve is shown in Fig. 2.

Note that the suggested S-curve compresses the signal intensity in the $[-30, 0]$-dB interval, effectively making the light regions more uniform, and stretches the DR from -30 dB and downward, effectively making the dark regions even darker.

III. MATERIALS AND METHODS

A. Image Quality Metrics

No clear consensus exists yet on how to measure the contrast of ultrasound images. Perhaps, the most widespread definition [14], [23], [27] is the one in [28]

$$CR = \frac{\mu_{ROI}}{\mu_B} \qquad (26)$$

where $\mu = E\{|b|^2\}$ is the expected value of the power of the beamformed signal, in the linear scale, over a certain region; and where ROI and B denote, respectively, a region of interest and a background region. If the signal power is proportional to the backscattering coefficient, which is the case for speckle signals beamformed with DAS, then CR is proportional to the ratio of the particle concentration in both regions. CR, often referred to as contrast ratio, can be expressed in the logarithmic scale as

$$CR[dB] = 10 \log_{10} CR. \qquad (27)$$

Detection probability not only depends on the mean value of the signal power but also on its variance. An alternative measure of contrast can be found in [29], a measure that became later known as the contrast-to-noise ratio

$$CNR = \frac{|\mu_{ROI} - \mu_B|}{\sqrt{\sigma_{ROI}^2 + \sigma_B^2}} \qquad (28)$$

where $\sigma = \sqrt{E\{(|b|^2 - \mu)^2\}}$ is the standard deviation of the power of the beamformed signal, in the linear scale. CNR is an estimate of the detection probability of a lesion. In particular, for the case of circularly symmetric Gaussian-distributed signals, which is the case of speckle signals beamformed with DAS, CNR is bounded to the interval [0, 1]. This metric has been used by many authors [14], [16], [23], [27].

Even though (26) and (28) were originally proposed to be applied to signal power in natural units, many authors have chosen to insert log-compressed values in them, effectively defining the alternative metrics

$$CR_{LC}[dB] = |\tilde{\mu}_{ROI} - \tilde{\mu}_B| \qquad (29)$$

where $\tilde{\mu} = E\{20 \log_{10}(|b|)\}$ is the expected value of the log-compressed values within the ROI and B regions, and

$$CNR_{LC}[dB] = \frac{|\tilde{\mu}_{ROI} - \tilde{\mu}_B|}{\sqrt{\tilde{\sigma}_{ROI}^2 + \tilde{\sigma}_B^2}} \qquad (30)$$

where $\tilde{\sigma} = \sqrt{E\{(20 \log_{10}(|b|) - \tilde{\mu})^2\}}$ is the standard deviation of the log-compressed signal within the ROI and B region. We include the subindex LC to denote the metrics computed on log-compressed values.

Although (29) is similar to (27), they are not identical since $10 \log_{10}(E\{|b|^2\}) \neq E\{20 \log_{10}(|b|)\}$. CNR and CNR_{LC} take completely different values and cannot be directly compared. Although both are thought to be estimates of the lesion detection probability, CR_{LC} can take values larger than 1, even for speckle signal beamformed with DAS. Several authors [13], [16], [22], [30], [31] have chosen (29) and (30) to quantify contrast.
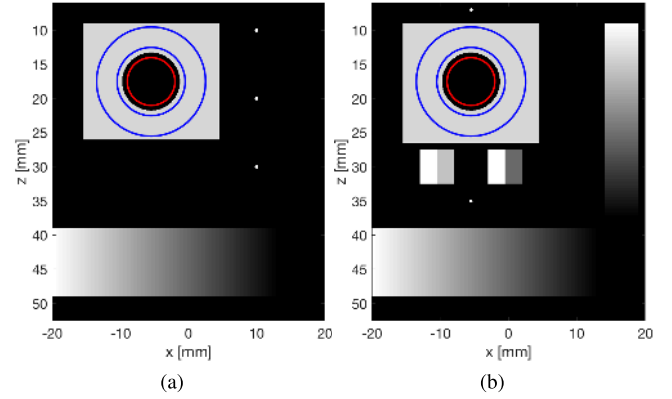

Fig. 3. (a) Experimental and (b) simulated DR phantoms shown with 60-dB DR.

In [14], [15], [17], [25], [26], and [32], it is not explicit whether logarithmic or natural units have been used. In some others, variations of the classical definitions are used [17], [22], [31].

B. Experimental Data

One element synthetic transmit aperture imaging (STAI) data sets are used. 204 STAI data sets were recorded with a Verasonics Vantage 256 system (Verasonics, Kirkland, WA, USA) and an L-11 linear array (128-element, 300-μm pitch) transmitting at 5.28 MHz. The probe was mounted on a 3-D position system Physik Instrumente [Physik Instrumente (PI) GmbH Co. KG, Karlsruhe, Germany] with a minimum incremental motion of 0.1 μm.

Several tissue mimicking targets were made following the instructions in Annex II of IEC60601-2-37 [33] and cut into the following shapes:

1) *T1:* A 20 × 17 mm block with a 8.5-mm-diameter circular hole,
2) *T2:* A 2 × 10 mm block.

In addition, a 200-μm nylon line was used as a wire target.

The targets were placed in a water tank at 23 °C. The 3-D positioning system allowed us to control the target relative position respect to the probe. Multiple data sets were recorded separately, in particular as follows.

1) A data set was recorded with T1 centered at (−5.5, 17.5) mm.
2) 200 data sets were recorded with T2 placed at $z = 44$ mm depth with x ranging from −20 to 20 mm to be combined into the lateral gradient.
3) Three additional data sets were recorded with the wire target at $x = 12$ mm and depth $z = [10, 20, 30]$ mm.

The 204 data sets were normalized in amplitude and combined into a single data set via weighted addition of RF channel data. Weights were selected so as to produce a final gradient of 1.8 dB/mm, covering the normalized range [0, −50] dB from −14 to 14 mm. Note that this operation is done on RF channel data and hence before any beamforming operation. The gradient from [0, −50] dB, −14 to 14 mm was selected to avoid unwanted effects from the edges of the image and ensure that the gradient was linear. The ROI used for

contrast estimation is shown in Fig. 3(a) circumscribed by the red circle, while the background area is shown between the two blue circles. The experimental data set is available for download from http://www.USTB.no/publications/dynamic_range/.

C. Simulated Data

A data set was generated using Field II [34], [35]. A 128-element, 300-μm pitch linear probe was simulated transmitting a 2.5-cycle Gaussian-modulated sinusoidal pulse with a center frequency of 5.13 MHz. Element height was set to $\lambda/2$ to produce a uniform field of view and rule out the effect of elevation focusing [36].

A phantom was designed to match the experimental data set as close as possible. The simulated phantom is shown in Fig. 3(b), consisting of point targets, a hypoechoic cystic region, and two bands with monotonically decreasing speckle intensity.

1) A 10-mm-wide lateral gradient at $z = 44$ mm depth, of 1.8 dB/mm covering a normalized scattering intensity range of $[0, -50]$ dB from $x = -14$ mm to $x = 14$ mm.
2) A 5-mm-wide axial gradient at $x = 16.5$ mm in the azimuth direction, of 1.8 dB/mm covering a normalized scattering intensity range of $[0, -50]$ dB from $z = 10$ to $z = 39$ mm. The axial gradient is not present in the experimental data.

In addition, and different from the experimental data set, four rectangular speckle regions are placed at $z = 30$ mm depth with intensities 0, −10, 0, and −35 dB to help the discussion of the results. We ensure well developed speckle [37] using 650 scatterers per mm³. The scatters are placed on a 2-D plane using Gaussian random amplitude to mimic positions in elevation. The ROI used for the contrast estimation is circumscribed by the red circle in Fig. 3(b), while the background region is that between the two blue circles. The simulated data set can be downloaded from http://www.USTB.no/publications/dynamic_range/.

D. Data Processing

Both the simulated and experimental data sets were beamformed with the UltraSound ToolBox (USTB) [38] using a dynamic expanding aperture with F number 1.75 and a rectangular window, both in transmit and receive.

All the transmit signals were delayed and combined to produce globally focused images. The beamformers described in Section II were applied only on the receive channels.

Some of the algorithms have user-settable parameters. For MV, L was set to 50% of the active receive channels, $K = 1.5\lambda$, and a diagonal loading factor of $\Delta = 1/100$ was used as suggested in [21]. The number of eigenvectors used in EBMV was selected adaptively using the eigenvectors with eigenvalues larger than $\delta = 0.5$ times the maximum eigenvalue as suggested in [22]. For GCF, the value $M_0 = 2$ was used as suggested in [25]. For PCF, $\gamma = 1$ was chosen as suggested in [26]. For the S-curve in the GLT algorithm, we used $\alpha = 0.12$, $\beta = -40$, and $\epsilon = 0.008$.

The sound speed in the simulation was 1540 m/s, while for the experimental data set, 1470 m/s was used. All images

were compensated to obtain uniform speckle intensity in the whole field of view. This was done differently in the simulated and experimental data. In the simulation, an analytical compensation was used that accounted for the focal depth and element directivity. Details on this compensation are given in [36] together with data and code. In the experiment, the compensation was carried out empirically. A uniform block of Agar was imaged, with fully developed speckle, and the estimated intensity field was spacially averaged and inverted. Both processes could be seen as a software time gain compensation performed on a uniform reference.

The beamforming grid was 1024 × 2048 pixels to cover the demands of F-DMAS in the axial direction, since F-DMAS produce a frequency component at $2f_c$, and of MV in the lateral direction [39]. The code used to beamform the images and reproduce all the results in this manuscript is available at http://www.USTB.no/publications/dynamic_range/ for MATLAB (The MathWorks, Natick, MA, USA).

E. Dynamic Range Test (DRT)

With gradients in both the simulated and experimental data set, we can define a DRT as

$$\text{DRT} = \frac{\Delta}{\Delta_0} \quad (31)$$

where Δ denotes the gradient of a given beamforming method, estimated via linear regression, and Δ_0 denotes the theoretical gradient, as fixed in the simulated and experimental data. DRT measures how many decibels the output DR deviates from the theoretical, for each decibel of the input DR.

For the simulated data set, we have both an axial and a lateral gradient and DRT can be estimated for both. For simplicity, the reported DRT value will be the average of the DRT in the axial and lateral directions. For the experimental data set, DRT is estimated in the lateral gradient.

The data sets and code to perform the test are available at http://www.USTB.no/publications/dynamic_range/.

IV. RESULTS

The images produced by all the methods in Section II are shown in Fig. 4, for both simulated [Fig. 4(a)–(h)], and experimental [Fig. 4(i)–(p)] data.

Fig. 5 shows the contrast of the hypoechoic cyst, for both simulated and experimental data, using the metrics in Section III-A and for all methods under study. As expected, we observe a good correlation between CR and CR_{LC} for all methods and data type, while CNR and CNR_{LC} are not obviously correlated.

The method showing the highest CR and CR_{LC} is GLT followed by EBMV, CF, or PCF. GLT also shows the best CNR, followed by DAS and GCF. GLT has the highest CNR_{LC} followed by EBMV and MV.

To study how each of the studied methods altered the DR, the mean intensity profile along the gradients was computed, and it is shown in Fig. 6. Simulated and experimental data are plotted in the same figure against the ground truth.

In general, we see a good agreement between the simulated and experimental results. As expected, DAS follows
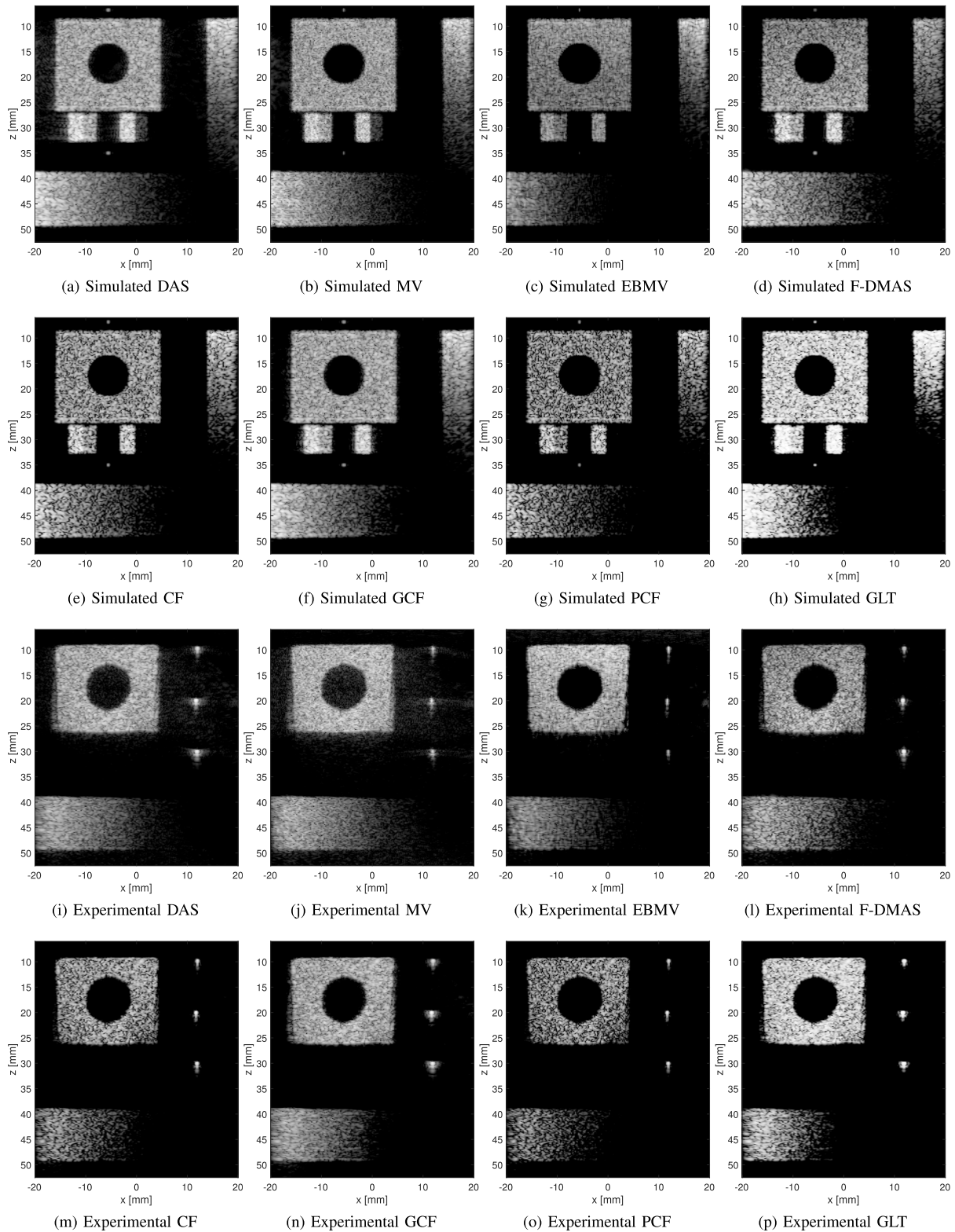
Fig. 4. Images of the simulated phantom (a–h) and the experimental phantom (i–p) for all beamformers under study. The images are shown with 60-dB dynamic range.

the ground truth closely. MV shows also a good agreement, while EBMV abruptly drops at -30 dB. F-DMAS shows a slight compression of the DR within 0 and -25 dB, and DR stretching from -25 dB and downward. The other adaptive beamformers (CF, GCF, and PCF) show a similar output DR that stretches the DR from -20 dB and downward.

To illustrate how DR transformations can affect the visibility of clinically relevant structures, we included four speckle
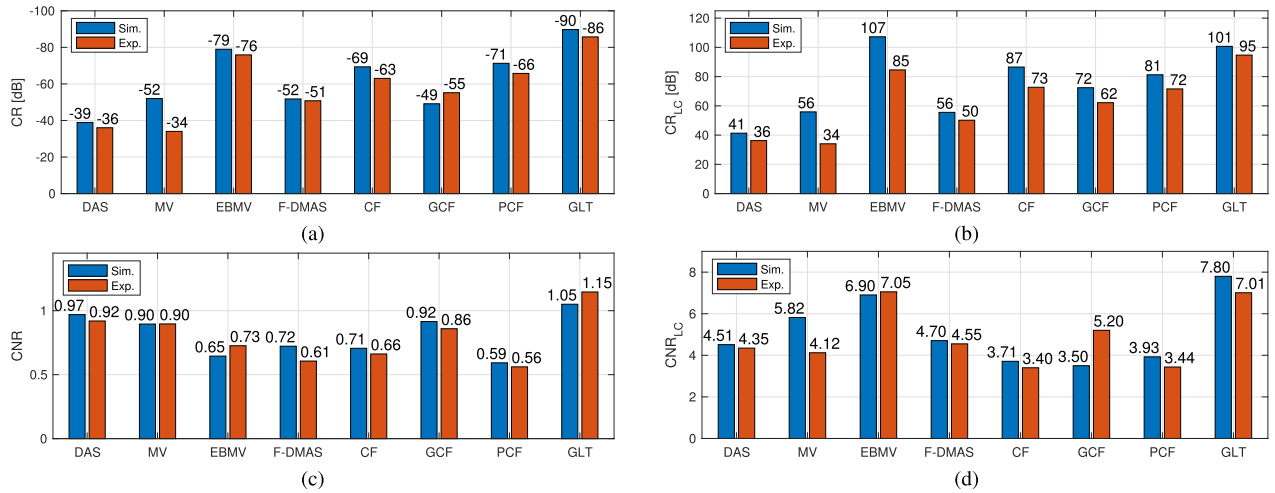
Fig. 5. Measured contrast of the simulated and the experimental hypoechoic cyst at $(-5.5, 17.5)$ mm using all contrast metrics as defined in Section III-A. (a) CR. (b) CR_{LC}. (c) CNR. (d) CNR_{LC}.
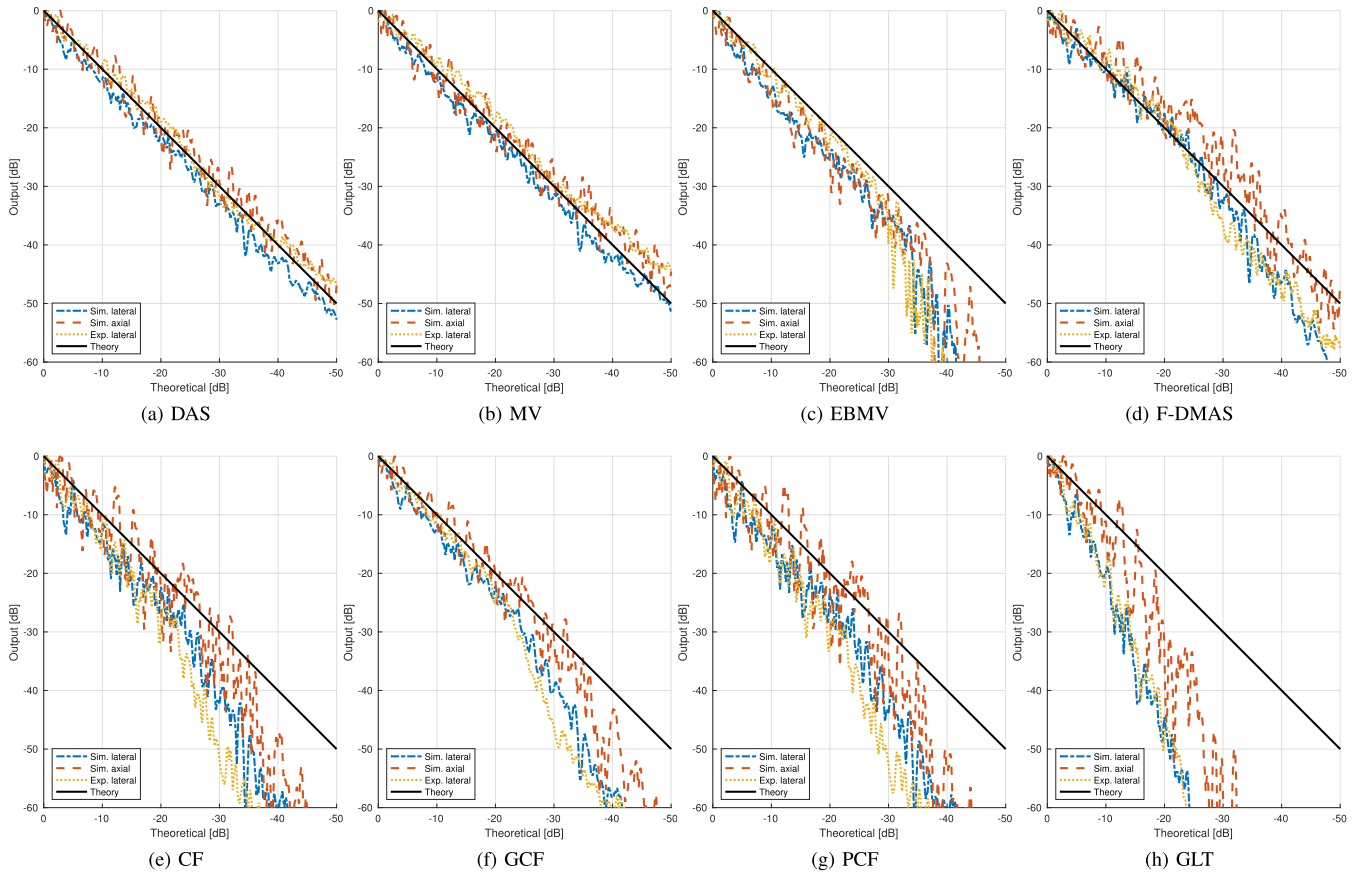

Fig. 6. The normalized average response of both the axial and lateral gradient for the simulation and the lateral gradient for the experimental data plotted against the theoretical response. The simulated axial gradient is measured between $z = 10$ mm and $z = 38$ mm, while the simulated and experimental lateral gradient is measured between $x = -14$ mm and $x = 14$ mm.

regions in the simulated phantom, with backscattering intensity of 0, -10, 0, and -35 dB, as shown in Fig. 7(a)–(h) in a 60-dB DR. The average lateral response through the speckle regions are shown in Fig. 8. The four speckle regions are easily observed in the DAS and MV images. The visibility of the -35-dB region is significantly reduced in the F-DMAS, GCF,

and GLT images; while the region is completely removed in the EBMV, CF, and PCF images.

For completeness, we have included examples of the full DRT defined in Section III-E for DAS, EBMV, and CF for the simulated data set in Fig. 9(a)–(c) and the experimental data set in Fig. 9(d)–(f). The region used to estimate the

(a) DAS   (b) MV   (c) EBMV   (d) F-DMAS

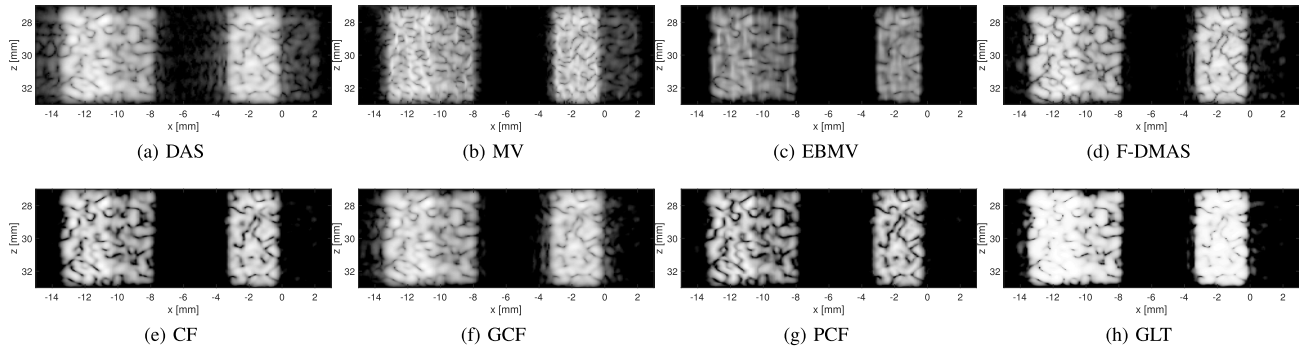(e) CF   (f) GCF   (g) PCF   (h) GLT

Fig. 7. Enlarged images of part of the simulated image containing speckle regions with two smaller speckle regions with a difference in echogenicity of 10 dB, left, and 35 dB, right. The images are shown with 60 dB dynamic range. Notice, that the speckle region between $x = -0.5$ and $x = 2$ mm is present in the DAS and MV image, partly visible in the F-DMAS, GCF and GLT image but completely gone for EBMV, CF, and PCF image.
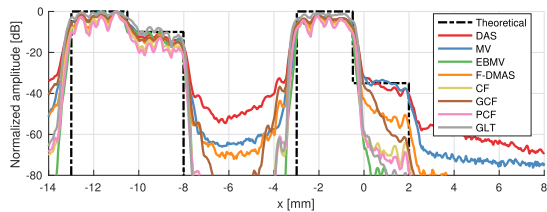

Fig. 8. Average lateral response through the speckle regions shown in Fig. 7.

gradient is indicated with the dashed color in the B-mode image and plotted in the subplot with the corresponding color. The theoretical and estimated gradients are in the subplot. In Fig. 9(g), the DRT values, the ratio between the estimated and the theoretical gradient, is plotted for all beamformers.

V. DISCUSSION

All the studied adaptive beamformers produce higher CR than DAS as measured by (26) or (29), with the exception of MV which only improves the contrast in the simulated case. However, one can get an arbitrarily high contrast using the trivial GLT, as shown in Fig. 5(a) and (b). This proves that higher CR does not necessarily mean better image quality or better lesion detection.

Using the classical definition of CNR given in (28), we observe that GLT holds the highest value. Again, this proves the point that a trivial transformation of DR can lead to increased CNR values.

If the definition in (30) is used, GLT has a slightly higher value than EBMV. This proves that DR transformations can alter the estimation of CNR, and that a higher CNR does not necessarily mean better lesion detectability.

Using the suggested DRT, we observe that EBMV, F-DMAS, CF, GCF, PCF, and GLT all produce DR stretching. This is evident from Fig. 6 where we observe that only the DAS and MV follow the linear drop of the horizontal intensity gradient. The test reveals the DR transformation curves associated with each technique: EBMV has an abrupt drop between -30 and -35 dB; whereas, F-DMAS, CF, GCF, PCF, and GLT have a parabolic curve that stretches the region below -20 dB. We observe that the gradient of the curve is notably smaller for F-DMAS, which fits the findings in [40].

From the examples of the DRT in Fig. 9, and the resulting gradients in Fig. 6, we can observe that the resulting gradients for most of the beamformers seem to be of higher orders than a linear line. However, a linear line is suitable as an intuitive indicator to determine if a beamformer is alternating the DR. Thus, the DRT values, plotted in Fig. 9(g), provide a quantitative indication of the DR alteration of the beamformer. It should also be mentioned that the selected DR of the gradient will affect the resulting DRT values and that we chose the largest DR possible while still maintaining a linear gradient in the experimental data.

We observe that the increase in CR_{LC} with respect to that of DAS seems to be correlated with the amount of DR stretching as measured by the DRT. Fig. 10 shows the DRT value, for all the methods except GLT, versus the CR_{LC} improvement compared to DAS. We observe that R^2-adj $= 0.88$ (0.72 when including the GLT) for simulated data and R^2-adj $= 0.98$ (0.98 when including the GLT) for experimental data. This indicates that CR enhancement in the tested algorithms may be merely due to DR stretching. The GLT curve was chosen to fit the experimental results, and this choice probably explains the lower R^2-adj for the simulated data.

In [20], we suggested that DR transformations could be compensated by a calibration of the beamformed images, using the gradient response. In [20], we tested this approach on several algorithms and observed a dramatic reduction in CR improvement. However, even though known phantoms can be calibrated, adaptive beamformers can produce DR transformations that are dependent on the structures in the image. In other words, the DR transformation curve of an adaptive beamformer is often image-dependent: it can differ from patient to patient, from organ to organ, or even between areas of the same image. This is illustrated in Fig. 11. In Fig. 11(a), the estimated gradient is shown for all methods after compensation, producing perfect linear slopes as expected. However, if we observe the intensity of the block along the depth $z = 30$ mm, in Fig. 11(b), we see that the calibrated signals still differ from the theoretical for some of the methods.

This can be explained. The pixel intensity produced by coherent-based methods, such as CF, PCF, and GCF, is highly dependent on the ratio of coherent to incoherent energy, which in turn depends on the slope of the gradient. In gradients that
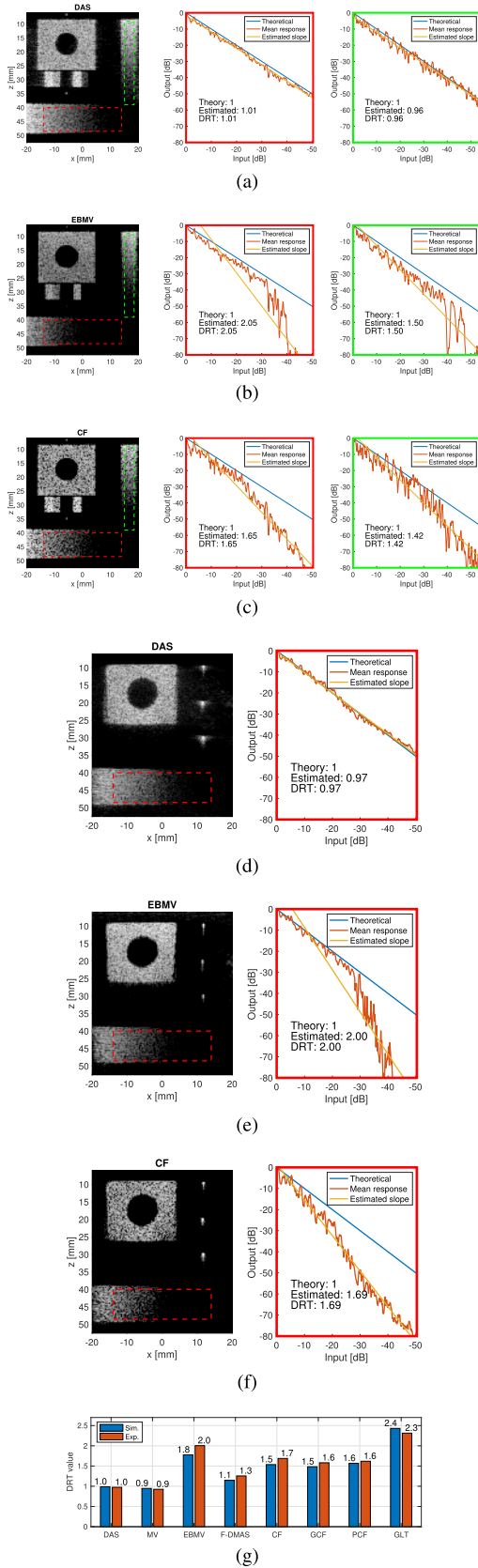
Fig. 9.   Examples of the DRT defined in Section III-E. (a)–(c) DAS, EBMV, and CF on the simulated data set, while (d)–(f) on experimental data. (g) Resulting DRT value for all beamformers.

change slowly, along the lateral direction, this ratio will be larger than in gradients that change more abruptly. Hence,
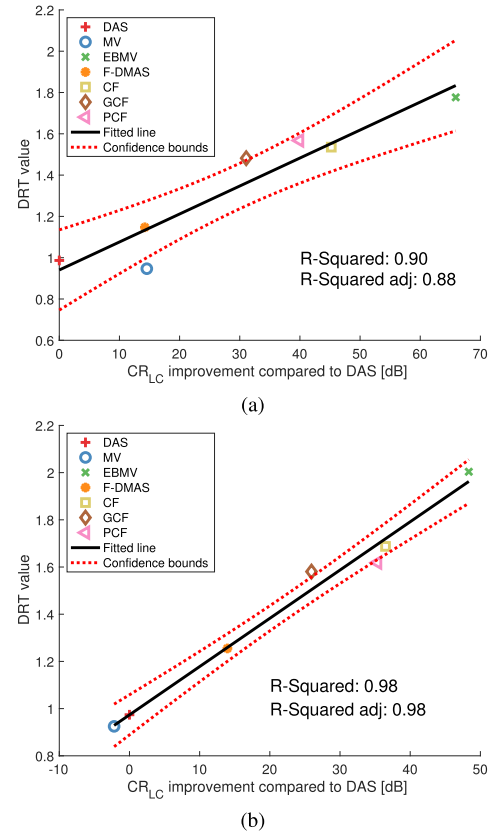

Fig. 10.   Improvement in CR_{LC} compared to DAS plotted against the DRT value which is the ratio between the estimated and the theoretical gradient. The results from the (a) simulated and (b) experimental data.
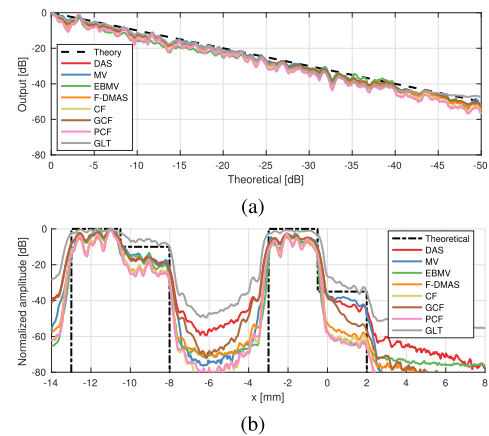

Fig. 11.   (a) Simulated lateral gradient after calibration is plotted. (b) Response through the speckle regions as in Fig. 8 but after calibration.

it becomes then impossible to find a single calibration curve for the whole image and for the whole algorithm.

Consider the phantom in Fig. 12(a) where only the axial gradient is included. Fig. 12(b) shows the DR transformation curves for DAS, CF, GCF, F-DMAS, MV, EBMV, and PCF. Note that, in this case, all beamformers leave the output DR almost unaltered. We must then conclude that it is the presence of the other structures, in the lateral direction, that induces DR stretching. Based on these two results, we now
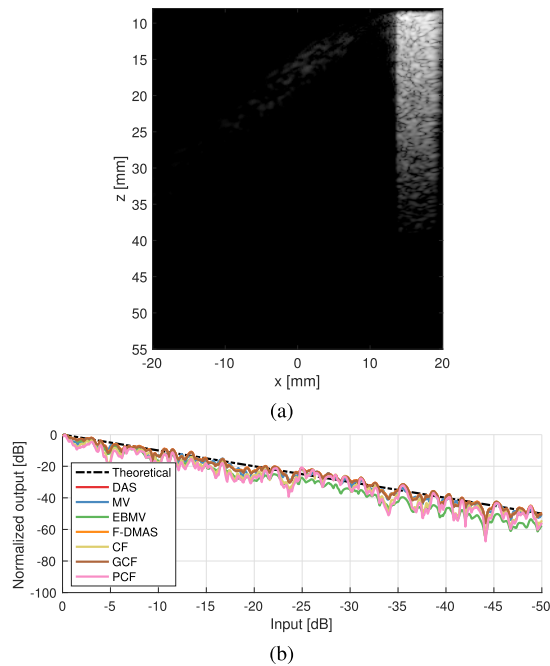
Fig. 12.   (a) DAS image of the simulated phantom with all other elements of the phantom removed but the axial gradient. (b) Average response of the axial gradient, when only the axial gradient is present in the image, is plotted for all beamformers.

believe, contrary to in [20], that compensating for the effect is extremely difficult, if not impossible.

Even though we cannot correct DR transformations, it is important to be aware of its consequences. The images in Figs. 7 and 8 illustrated that DR stretching can lead to some information not being displayed, information that could be clinically relevant. In most cases that information could be recovered if the image is displayed using a different dynamic scale, but that will also reduce the apparent *visual* contrast that seems to correlate with the increase in C and CNR values.

We showed that DR transformation makes any estimation of CR and CNR questionable, and given that some adaptive beamformers transform the output DR, it follows that claims on lesion detectability based on CR and CNR estimates should be revised. We have introduced data sets and code making it possible to investigate whether and how much a beamforming method is alternating the DR.

The results presented here expose a dangerous weakness of our image quality metrics. This weakness must be remediated. We must lay the groundwork upon which we build the new techniques. A new metric for contrast must be sought, one that is immune to DR transformations, and help us assess the relevance of present and future beamforming techniques.

VI. Conclusion

We propose a dynamic range test to estimate the output dynamic range of any beamforming algorithm. This test, comprising data and code, is made publicly available through the UltraSound ToolBox (USTB, http://www.ustb.no/ publications/dynamic_range/), allowing anyone to check if an algorithm transforms the output DR of the beamformed images.

We applied the proposed test to several state-of-the-art algorithms: DAS, MV, EBMV, F-DMAS, CF, GCF, and PCF. We show that some state-of-the-art beamformers alter the DR either by compressing it, by stretching it, or by a combination of both. The amount of dynamic range alteration, as measured by the dynamic range test, correlates the CR improvement with R^2-adj $= 0.88$ for the simulated data and R^2-adj $= 0.98$ for the experimental data.

Our results show that improvements in CR and CNR can, for some beamformers, be explained by a stretching of the dynamic range. Thus, claims on lesion detectability based on the CR and CNR metrics should be revised, and metrics immune to dynamic range alterations should be sought.

References

[1] F. Bryn, "Optimum signal processing of three-dimensional arrays operating on Gaussian signals and noise," *J. Acoust. Soc. Amer.*, vol. 34, no. 3, pp. 289–297, Mar. 1962.

[2] B. Widrow, P. E. Mantey, L. J. Griffiths, and B. B. Goode, "Adaptive antenna systems," *Proc. IEEE*, vol. 55, no. 12, pp. 2143–2159, Dec. 1967.

[3] S. Applebaum, "Adaptive arrays," *IEEE Trans. Antennas Propag.*, vol. AP-24, no. 5, pp. 585–598, Sep. 1976.

[4] J. Capon, "Optimum weighting functions for the detection of sampled signals in noise," *IEEE Trans. Inf. Theory*, vol. IT-10, no. 2, pp. 152–159, Apr. 1964.

[5] S. W. Flax and M. O'Donnell, "Phase-aberration correction using signals from point reflectors and diffuse scatterers: Basic principles," *IEEE Trans. Ultrason., Ferroelectr., Freq. Control*, vol. 35, no. 6, pp. 758–767, Nov. 1988.

[6] L. Nock, G. E. Trahey, and S. W. Smith, "Phase aberration correction in medical ultrasound using speckle brightness as a quality factor," *J. Acoust. Soc. Amer.*, vol. 85, no. 5, pp. 1819–1833, May 1989.

[7] J. A. Mann and W. F. Walker, "A constrained adaptive beamformer for medical ultrasound: Initial results," in *Proc. IEEE Ultrason. Symp.*, vol. 2, Oct. 2002, pp. 1807–1810.

[8] M. Sasso and C. Cohen-Bacrie, "Medical ultrasound imaging using the fully adaptive beamformer," in *Proc. IEEE Int. Conf. Acoust., Speech, Signal Process., (ICAASP).*, vol. 2, Mar. 2005, pp. 489–492.

[9] F. Viola and W. Walker, "Adaptive signal processing in medical ultrasound beamforming," in *Proc. IEEE Ultrason. Symp.*, vol. 4, Sep. 2005, pp. 1980–1983.

[10] Z. Wang, J. Li, and R. Wu, "Time-delay- and time-reversal-based robust capon beamformers for ultrasound imaging," *IEEE Trans. Med. Imag.*, vol. 24, no. 10, pp. 1308–1322, Oct. 2005.

[11] J. Synnevåg, A. Austeng, and S. Holm, "Minimum variance adaptive beamforming applied to medical ultrasound imaging," in *Proc. IEEE Ultrason. Symp.*, vol. 2, Sep. 2005, pp. 1199–1202.

[12] *Scopus Document Search Results*. Accessed: Feb. 21, 2018. [Online]. Available: https://www.scopus.com

[13] N. Q. Nguyen and R. W. Prager, "A spatial coherence approach to minimum variance beamforming for plane-wave compounding," *IEEE Trans. Ultrason., Ferroelectr., Freq. Control*, vol. 65, no. 4, pp. 522–534, Apr. 2018.

[14] J. Zhao, Y. Wang, J. Yu, W. Guo, S. Zhang, and S. Aliabadi, "Short-lag spatial coherence ultrasound imaging with adaptive synthetic transmit aperture focusing," *Ultrason. Imag.*, vol. 39, no. 4, pp. 224–239, Jul. 2017.

[15] B. Zhuang, R. Rohling, and P. Abolmaesumi, "Accumulated angle factor-based beamforming to improve the visualization of spinal structures in ultrasound images," *IEEE Trans. Ultrason., Ferroelectr., Freq. Control*, vol. 65, no. 2, pp. 210–222, Feb. 2018.

[16] J. Shin and L. Huang, "Spatial prediction filtering of acoustic clutter and random noise in medical ultrasound imaging," *IEEE Trans. Med. Imag.*, vol. 36, no. 2, pp. 396–406, Feb. 2017.

[17] E. Ozkan, V. Vishnevsky, and O. Goksel, "Inverse problem of ultrasound beamforming with sparsity constraints and regularization," *IEEE Trans. Ultrason., Ferroelectr., Freq. Control*, vol. 65, no. 3, pp. 356–365, Mar. 2018.

[18] T. Szasz, A. Basarab, and D. Kouamé, "Beamforming through regularized inverse problems in ultrasound medical imaging," *IEEE Trans. Ultrason., Ferroelectr., Freq. Control*, vol. 63, no. 12, pp. 2031–2044, Dec. 2016.

[19] S. W. Smith, R. F. Wagner, J. M. Sandrik, and H. Lopez, "Low contrast detectability and contrast/detail analysis in medical ultrasound," *IEEE Trans. Sonics Ultrason.*, vol. 30, no. 3, pp. 164–173, May 1983.

[20] O. M. H. Rindal, A. Austeng, H. Torp, S. Holm, and A. Rodriguez-Molares, "The dynamic range of adaptive beamformers," in *Proc. IEEE Int. Ultrason. Symp. (IUS)*, vol. 1, Sep. 2016, pp. 1–4.

[21] J.-F. Synnevag, A. Austeng, and S. Holm, "Benefits of minimum-variance beamforming in medical ultrasound imaging," *IEEE Trans. Ultrason., Ferroelectr., Freq. Control*, vol. 56, no. 9, pp. 1868–1879, Sep. 2009.

[22] B. M. Asl and A. Mahloojifar, "Eigenspace-based minimum variance beamforming applied to medical ultrasound imaging," *IEEE Trans. Ultrason., Ferroelectr., Freq. Control*, vol. 57, no. 11, pp. 2381–2390, Nov. 2010.

[23] G. Matrone, A. S. Savoia, G. Caliano, and G. Magenes, "The delay multiply and sum beamforming algorithm in ultrasound B-mode medical imaging," *IEEE Trans. Med. Imag.*, vol. 34, no. 4, pp. 940–949, Apr. 2015.

[24] R. Mallart and M. Fink, "Adaptive focusing in scattering media through sound-speed inhomogeneities: The van Cittert Zernike approach and focusing criterion," *J. Acoust. Soc. Amer.*, vol. 96, no. 6, pp. 3721–3732, Dec. 1994.

[25] P. C. Li and M. L. Li, "Adaptive imaging using the generalized coherence factor," *IEEE Trans. Ultrason., Ferroelectr., Freq. Control*, vol. 50, no. 2, pp. 128–141, Feb. 2003.

[26] J. Camacho, M. Parrilla, and C. Fritsch, "Phase coherence imaging," *IEEE Trans. Ultrason., Ferroelectr., Freq. Control*, vol. 56, no. 5, pp. 958–974, May 2009.

[27] M. A. Lediju, G. E. Trahey, B. C. Byram, and J. J. Dahl, "Short-lag spatial coherence of backscattered echoes: Imaging characteristics," *IEEE Trans. Ultrason., Ferroelectr., Freq. Control*, vol. 58, no. 7, pp. 1377–1388, Jul. 2011.

[28] S. Smith, H. Lopez, and W. Bodine, "Frequency independent ultrasound contrast-detail analysis," *Ultrasound Med. Biol.*, vol. 11, no. 3, pp. 467–477, May/Jun. 1985.

[29] M. Patterson and F. Foster, "The improvement and quantitative assessment of B-mode images produced by an annular array/cone hybrid," *Ultrason. Imag.*, vol. 5, no. 3, pp. 195–213, Jul. 1983.

[30] S. Mehdizadeh, A. Austeng, T. F. Johansen, and S. Holm, "Eigenspace based minimum variance beamforming applied to ultrasound imaging of acoustically hard tissues," *IEEE Trans. Med. Imag.*, vol. 31, no. 10, pp. 1912–1921, Oct. 2012.

[31] S. Krishnan, K. W. Rigby, and M. O'Donnell, "Improved estimation of phase aberration profiles," *IEEE Trans. Ultrason., Ferroelectr., Freq. Control*, vol. 44, no. 3, pp. 701–713, May 1997.

[32] T. Szasz, A. Basarab, and D. Kouamé, "Strong reflector-based beamforming in ultrasound medical imaging," *Ultrasonics*, vol. 66, pp. 111–124, Mar. 2016.

[33] *Medical Electrical Equipment—Part 2–37: Particular Requirements for the Basic Safety and Essential Performance of Ultrasonic Medical Diagnostic and Monitoring Equipment*, Standard IEC 60601-2-37:2007, Geneva, Switzerland, Aug. 2007.

[34] J. A. Jensen and N. B. Svendsen, "Calculation of pressure fields from arbitrarily shaped, apodized, and excited ultrasound transducers," *IEEE Trans. Ultrason., Ferroelectr., Freq. Control*, vol. 39, no. 2, pp. 262–267, Mar. 1992.

[35] J. A. Jensen, "Field: A program for simulating ultrasound systems," presented at the 10th Nordic-Baltic Conf. Biomed. Imag. Published Med. Biol. Eng. Comput., vol. 34, 1996, pp. 351–353. [Online]. Available: https://field-ii.dk/?copyright.html

[36] O. M. H. Rindal. (2018). *Achieving Uniform Field of View (FOV) in Synthetic Aperture Imaging (STAI) in Field II Simulations*. [Online]. Available: http://www.ustb.no/examples/uniform-fov-in-field-ii-simulations/

[37] R. F. Wagner, M. F. Insana, and S. W. Smith, "Fundamental correlation lengths of coherent speckle in medical ultrasonic images," *IEEE Trans. Ultrason., Ferroelectr., Freq. Control*, vol. 35, no. 1, pp. 34–44, Jan. 1988.

[38] A. Rodriguez-Molares *et al.*, "The ultrasound toolbox," in *Proc. IEEE Int. Ultrason. Symp. (IUS)*, Sep. 2017, pp. 1–4.

[39] J. P. Åsen, A. Austeng, and S. Holm, "Capon beamforming and moving objects-an analysis of lateral shift-invariance," *IEEE Trans. Ultrason., Ferroelectr., Freq. Control*, vol. 61, no. 7, pp. 1152–1160, Jul. 2014.

[40] F. Prieur, O. M. H. Rindal, and A. Austeng, "Signal coherence and image amplitude with the filtered delay multiply and sum beamformer," *IEEE Trans. Ultrason., Ferroelectr., Freq. Control*, vol. 65, no. 7, pp. 1133–1140, Jul. 2018.

Ole Marius Hoel Rindal (S'14) was born in Norway in 1990. He received the M.S. degree in computer science (signal processing) from the University of Oslo, Oslo, Norway, in 2014, where he is currently pursuing the Ph.D. degree, with a focus on medical ultrasound beamforming techniques.

He also holds a position at the Centre for Elite Sports Research, Norwegian University of Science and Technology, Trondheim, Norway, doing research on signal processing on inertial measurement units used in cross-country skiing. His research interests include signal processing, medical image formation, image processing, machine learning, and physiological and biomechanical aspects of cross-country skiing.

Andreas Austeng (S'97–M'01–SM'16) received the M.S. degree in physics and the Ph.D. degree in computer science from the University of Oslo, Oslo, Norway, in 1996 and 2001, respectively.

Since 2001, he has been working at the Department of Informatics, University of Oslo, as a Post-Doctoral Research Fellow, an Associate Professor, and currently as a Professor with the Digital Signal Processing and Image Analysis Group. His research interests include signal processing for acoustical imaging and algorithms that aim to improve the quality of information extracted from images.

Ali Fatemi (GS'16) received the M.Sc. degree in medical technology from the Norwegian University of Science and Technology (NTNU), Trondheim, Norway, in 2015, with a focus on ultrasound imaging. He is currently pursuing the Ph.D. degree with the Department of Circulation and Medical Imaging (ISB), NTNU, with a focus on clutter generation mechanisms in cardiac ultrasound images and application of adaptive beamforming in cardiac ultrasound.

Alfonso Rodriguez-Molares (M'14) received the M.Sc. degree in telecommunications and the Ph.D. degree in signal processing and communication from the University of Vigo, Vigo, Spain, in 2006 and 2011, respectively.

He is an Associate Professor and a Senior Engineer with the Ultrasound Laboratory, Norwegian University of Science and Technology, Trondheim, Norway. He has coauthored over 15 papers in peer-reviewed journals. He holds two patents. His research interests include medical ultrasound, adaptive beamforming, acoustic propagation in heterogeneous media, and numerical acoustics.